IOP Publishing Journal of Micromechanics and Microengineering
J. Micromech. Microeng. 24 (2014) 125028 (9pp) doi:10.1088/0960-1317/24/12/125028

Hemispherical micro-resonators from atomic layer deposition

Jason M Gray[1], John P Houlton[2], Jonas C Gertsch[3], Joseph J Brown[1], Charles T Rogers[2], Steven M George[1,3] and Victor M Bright[1]

[1] Department of Mechanical Engineering, University of Colorado, Boulder, CO 80309, USA
[2] Department of Physics, University of Colorado, Boulder, CO 80309, USA
[3] Department of Chemistry and Biochemistry, University of Colorado, Boulder, CO 80309, USA

E-mail: jason.gray@colorado.edu

Received 31 July 2014, revised 28 October 2014
Accepted for publication 30 October 2014
Published 26 November 2014

Abstract
Hemispherical shell micro-resonators may be used as gyroscopes to potentially enable precision inertial navigation and guidance at low cost and size. Such devices require a high degree of symmetry and large quality factors (Q). Fabricating the devices from atomic layer deposition (ALD) facilitates symmetry through ALD's high conformality and low surface roughness. To maximize Q, the shells' geometry is optimized using finite element method (FEM) studies to reduce thermoelastic dissipation and anchor loss. The shells are fabricated by etching hemispherical molds in Si (1 1 1) substrates with a 2:7:1 volumetric ratio of hydrofluoric:nitric:acetic acids, and conformally coating and patterning the molds with ALD Al_2O_3. The Al_2O_3 shells are then released from the surrounding Si substrate with an SF_6 plasma. The resulting shells typically have radii around 50 μm and thicknesses close to 50 nm. The shells are highly symmetric, with radial deviations between 0.22 and 0.49%, and robust enough to be driven on resonance at amplitudes 10 × their thickness, sufficient to visualize the resonance mode shapes in an SEM. Resonance frequencies are around 60 kHz, with Q values between 1000 and 2000. This Q is lower than the 10^6 predicted by FEM, implying that Q is being limited by unmodeled sources of energy loss, most likely from surface effects or material defects.

Keywords: hemispherical shell resonator, atomic layer deposition, MEMS, finite element modeling

(Some figures may appear in colour only in the online journal)

1. Introduction

For over 30 years, macroscale hemispherical resonator gyroscopes (HRGs) have enabled precision inertial navigation and guidance, including millions of operating hours in space with 100% mission success [1]. The HRG consists of a highly symmetric hemispherical shell resonator that, upon rotation, transfers energy between two degenerate resonance modes due to the Coriolis force [2, 3]. This energy transfer causes the shell's standing vibration wave to precess, with a precession angle related to the rotation angle by a scale factor dependent on the mode of oscillation [4–7].

In recent years, there has been a push for the development of microscale HRGs, with the goal of providing equivalent performance to their macroscale counterparts at reduced cost and volume. The primary impediment to developing micro-HRGs has been fabrication: the HRG is a 3D structure, while most microfabrication processes are restricted to 2D or 2.5D [8]. Several techniques have been developed to address this fabrication challenge, including microscale glassblowing [9, 10] and conformal mold coating [11–13]. This work describes a conformal mold coating technique using atomic layer deposition (ALD), a fabrication process which is widely transferrable to any application requiring 3D, high aspect-ratio structures. ALD is a thin-film deposition technique involving a repeated sequence of self-limiting reactions [14] that allows for highly conformal [15], continuous [16], ultrathin (down to ~1 nm) [17] films with angstrom-level thickness control [18, 19]

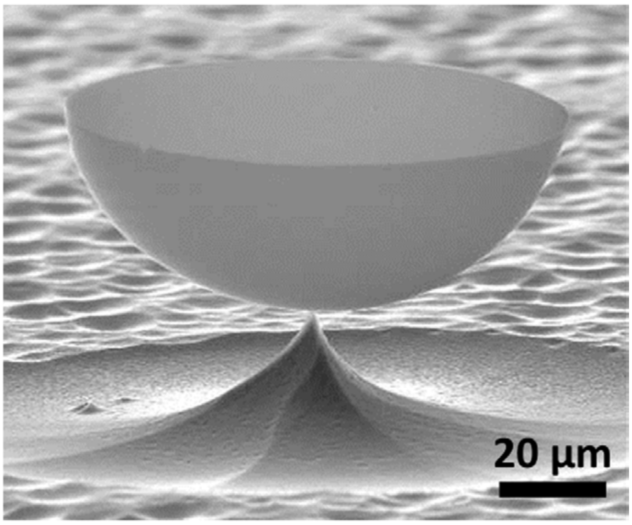

Figure 1. SEM micrograph of a 48 μm radius, 52 nm-thick Al_2O_3 wineglass resonator supported by a 0.6 μm radius Si stem.

and sub-nanometer surface roughness [20, 21]. In contrast to previous HRG studies that have used ALD as a coating layer [11], this work utilizes ALD as the sole device material.

The key performance requirements for the HRG include low resonance frequency mismatch, Δf, between the degenerate resonance modes (indicating a need for highly symmetric shells) and long resonance decay times, given by $\tau = Q/\pi f_0$ [22] (indicating a need for low resonance frequencies, f_0, and high quality factors, Q). ALD offers benefits for both of these requirements: for the former, the films' high conformality and low surface roughness minimize asymmetry due to film variation, while for the latter, the ultrathin thicknesses allow for lower f_0 and higher Q (due to the reduced impact of thermoelastic damping (TED)).

The effects of thickness and other geometry variations on f_0, Q due to TED, and Q due to anchor loss were modeled with finite element method (FEM) software. Using those modeling results as a guide, hemispherical shell resonators were designed and fabricated with ALD aluminum oxide (Al_2O_3), and their mechanical resonance properties measured. The resulting shells have radii typically around 50 μm, and thicknesses near 50 nm, as seen in figure 1. Both of these dimensions are one to two orders of magnitude smaller than similar devices [9–13], which have radii ranging from 370 μm to 2.5 mm and thicknesses from 1 to 10 μm.

2. Modeling

In order to design the geometry of the wineglass resonators to maximize Q and minimize f_0, extensive FEM modeling of the lowest-order wineglass mode ($n = 2$, figure 2) was performed using COMSOL Multiphysics software. Two degenerate modes exist at this frequency, where the standing wave of mode 1 is rotated by 45° compared to mode 2. Any asymmetries in the shell will cause frequency splitting between the two modes.

To model Q, the source of energy loss must be specified. Two of the most common sources of dissipation that wineglass resonators are likely to face are from anchor loss and TED [23]. Other sources of loss can include air damping, which is negligible when operating under vacuum, and surface effects, which are typically difficult to model and must often be measured empirically. To operate as precision gyroscopes, a Q of 10^6–10^7 is expected to be necessary.

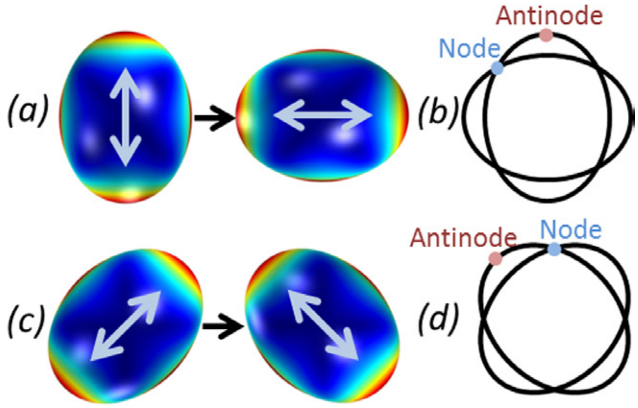

Figure 2. Overhead view of mode 1 (*a*) and mode 2 (*c*) of the $n = 2$ wineglass resonance, where red and blue regions indicate maximum and minimum displacements, respectively. The standing wave of mode 1 (*b*) is rotated 45° compared to the standing wave of mode 2 (*d*).

Q due to TED (Q_{TED}) was modeled as a function of thickness of the Al_2O_3 shell, using material properties from the literature (density = 3.0 g cm^{-3}, Young's modulus = 175 GPa, Poisson's ratio = 0.24 [24], coefficient of thermal expansion = 4.2 ppm °C^{-1} [25], thermal conductivity = 1.5 W m^{-1} K^{-1} [26], and heat capacity at constant pressure (for bulk Al_2O_3) = 730 J kg^{-1} K^{-1}). Q_{TED} was seen to increase with decreasing thickness, as expected from previous TED studies [22, 27]. The reduced impact of TED demonstrates an advantage of ultrathin ALD materials over thicker conventionally deposited materials. At 150 nm Al_2O_3 thickness, the model predicts $Q_{TED} = 1.5 \times 10^6$. Hence, with typical thicknesses around 50 nm, TED will likely be negligible.

Modeling Q due to anchor loss (Q_{anch}) was performed using the perfectly matched layer (PML) method, wherein acoustic energy lost through the anchor is absorbed by the PML, and the ratio of energy stored in the resonator over the energy lost in the PML is proportional to Q_{anch} [28]. The modeled geometry is shown in figure 3, where the parameters that were varied include shell radius r_s, anchor radius r_a, and shell thickness t. Anchor height h was also varied, but was found to have no impact on f_0 or Q_{anch}. The Al_2O_3 is meshed as a shell of 6000 mapped quadrilateral elements, the silicon mesh is ~150 000 solid tetrahedral elements (minimum size = 50 nm, maximum size = 5 μm), and the PML mesh is generated from sweeping the silicon mesh outwards radially.

The results of the FEM study are shown in figure 4. The shells were modeled as ALD Al_2O_3 with the same mechanical properties as given for the Q_{TED} study. The substrate was modeled as isotropic silicon (density = 2.329 g cm^{-3}, Young's modulus = 170 GPa, Poisson's ratio = 0.28) surrounded by a PML. A standard geometry was chosen, with $r_s = 50\,\mu$m, $r_a = 1\,\mu$m, and $t = 50$ nm. From these initial values, one parameter

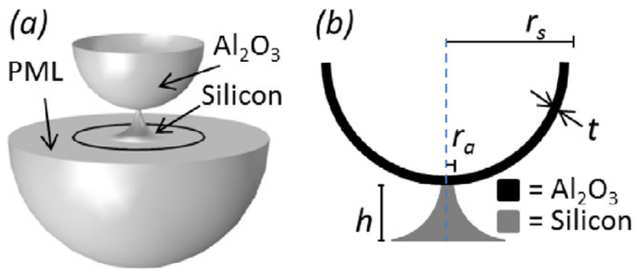

Figure 3. (*a*) Wineglass model with a perfectly matched layer (PML) used for anchor loss simulations with COMSOL. (*b*) Cross-section of the model with its associated variable geometric parameters: shell radius r_s, anchor radius r_a, shell thickness t, and anchor height h.

was varied at a time. The resulting influences on f_0 and Q_{anch} can be summarized as follows:

- *Anchor radius*: has the strongest influence of any parameter on f_0 and Q_{anch}. Increasing r_a from 1 to >7 μm causes Q_{anch} to drop from 10^6 to 100. For $r_a > 5\,\mu$m, the anchor begins contributing to the resonator's effective stiffness, increasing f_0.
- *Shell radius*: the second leading contributor to f_0 and Q_{anch}, where increasing r_s improves performance by decreasing f_0 and increasing Q_{anch}. For $r_s > \sim 50\,\mu$m, Q_{anch} rises above 10^6.
- *Shell thickness*: f_0 is directly proportional to t, whereas Q_{anch} displays a very small, nonlinear dependence with a peak at ~50 nm. This peak perhaps arises from the interaction between the thickness-dependent phonon mean free path and relaxation time, analogous to the thickness-dependent peak in Q predicted by Kunal and Aluru [29] due to Akhiezer damping.

Because simplifications have been taken in the construction of this model, it is important to note that this computational analysis should not be used for quantitative Q_{anch} predictions[4]. Expecting that the qualitative trends are still valid, the computational analysis provides qualitative design rules regarding the variables discussed above. The general design rules for achieving the highest possible Q are to minimize the anchor radius and maximize the shell radius. From these modeling results, the targeted geometric parameters for fabrication are chosen to be $t = 50$ nm, $r_s > 50\,\mu$m, and $r_a < 1\,\mu$m. For these parameters, FEM predicted both Q_{anch} and Q_{TED} to be $> 10^6$, with the caveats noted above.

3. Fabrication

The fabrication process flow for the wineglass resonators is provided in figure 5. A Cr/Au (20 nm/180 nm) mask is patterned with circular openings over a silicon substrate (*a*).

[4] For example, modeling of anchor loss using the PML method is known to lack accuracy when the model dimension is smaller than the acoustic wavelength, which is the case here (the acoustic wavelength of silicon is about 200 mm at 50 kHz). The assumption of unstressed, isotropic materials with smooth surfaces may also affect the calculation of wave propagation through the model.

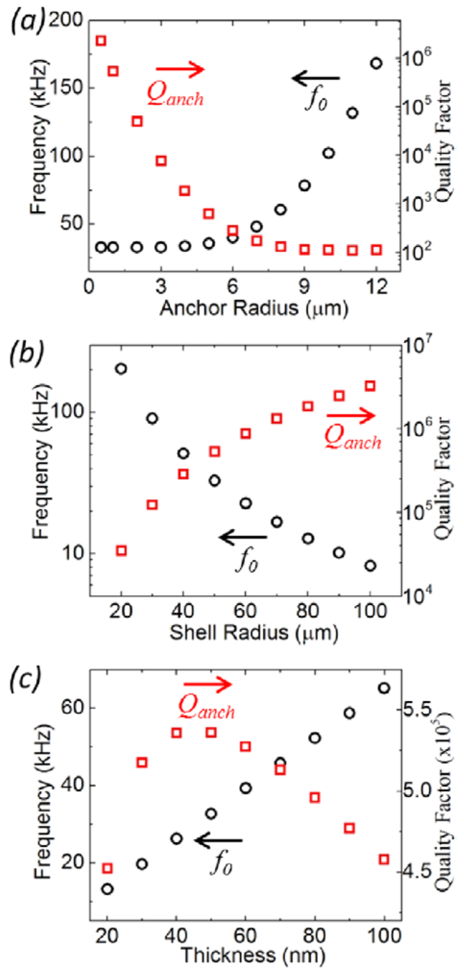

Figure 4. Simulation results of resonance frequency (circles, left axis) and Q_{anch} (squares, right axis) as a function of anchor radius (*a*), shell radius (*b*), and ALD Al_2O_3 thickness (*c*).

Hemispherical molds are etched in the substrate, either with SF_6 plasma or HNA (hydrofluoric, nitric, and acetic acids) (*b*). The wafer is coated with ALD Al_2O_3 (*c*). A thick photoresist is spun on and etched back, planarizing the molds. The Al_2O_3 is etched with buffered HF, leaving only the Al_2O_3 protected by photoresist in the molds (*d*). Finally, the silicon is etched back in an SF_6 plasma, leaving the ALD shell supported by a silicon stem (*e*). This fabrication can be summarized in three principal steps: (1) mold fabrication, (2) ALD shell definition, and (3) shell release.

3.1. Mold fabrication

The hemispherical mold is of critical importance to device performance, as the conformal nature of ALD means the shell will reproduce the mold shape with high fidelity. Hence, the mold must be smooth and symmetric to avoid any anisotropy that would increase the resonance frequency mismatch between degenerate resonance modes. As seen in figure 6, the symmetry and roughness of the molds are strongly dependent on the composition of the etchant and the etch conditions.

Initially, the molds were etched with an SF_6 plasma. While changing the etching parameters (including gas flow rate,

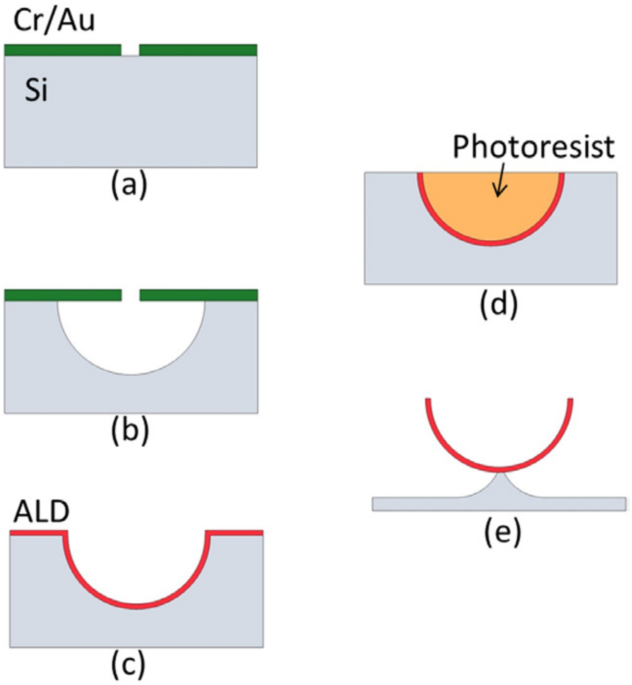

Figure 5. Fabrication process flow.

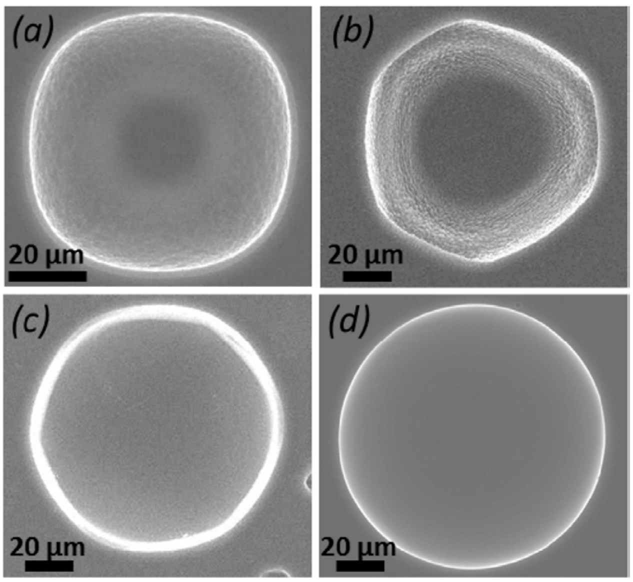

Figure 6. (*a*) SF_6-etched mold in Si (1 0 0). (b) SF_6-etched mold in Si (1 1 1). (*c*) HNA-etched mold in Si (1 1 1) at room temperature with no agitation. (*d*) HNA-etched mold in Si (1 1 1) at 50 °C with light agitation.

pressure, plasma power, and mask material) could change the isotropy and surface roughness of the mold, no set of parameters was found to provide adequate results. The resulting molds displayed crystal orientation dependence associated with the Si substrate's crystal planes, with Si (1 0 0) wafers producing square molds and Si (1 1 1) wafers producing hexagonal molds, as seen in (*a*) and (*b*) of figure 6.

With SF_6 discarded as a suitable etchant, HNA was chosen as a potential replacement. Schwartz and Robbins [30] showed that the isotropy and surface roughness of the HNA etch is highly dependent on the volume ratio of the three acids. Following the recommendation of [30] and Hamzah *et al* [31], a volumetric ratio of 2:7:1 hydrofluoric:nitric:acetic acids was chosen. The solution temperature and sample agitation also impact the resulting etched profile. Figure 6(*c*) shows the results of an HNA etch with an uncontrolled temperature starting from room temperature and no agitation, causing rim discoloration and noticeable crystal orientation dependence. After experimenting with temperature and agitation, figure 6(*d*) shows the final optimized recipe, performed at 50 °C with light, uniform agitation, displaying no obvious crystal orientation dependence and low surface roughness.

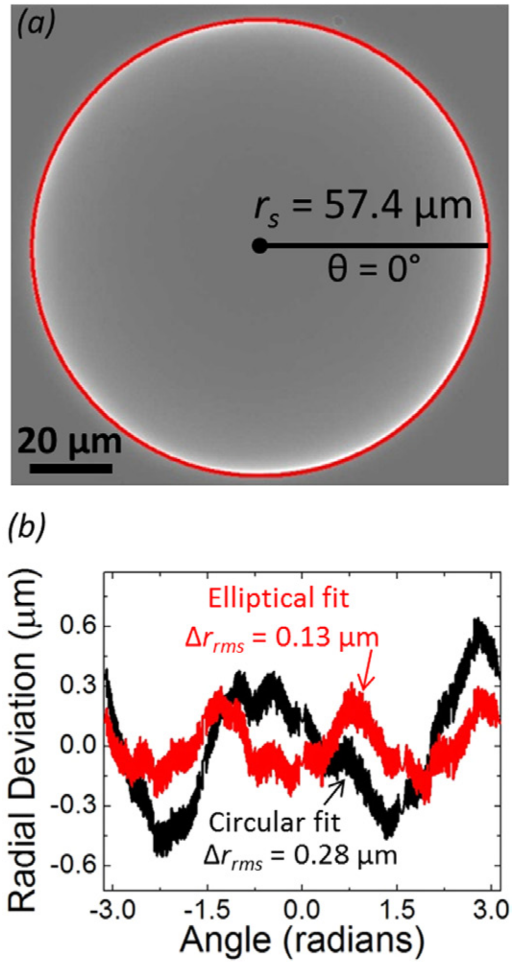

Figure 7. (*a*) Overhead SEM micrograph of a hemispherical mold with an overlaid fit to the mold's edge. (*b*) Radial deviation of the fit assuming a circular mold (black line) or elliptical mold (red line). The elliptical fit is intended to remove the error introduced by any potential tilt of the overhead image, and produces a lower root mean square (RMS) deviation.

To quantify the symmetry of the molds, a circular fitting algorithm was developed. First, the overhead SEM image of the mold is run through Mathematica's edge detection function. Then the resulting edge is fit to a circle and the radial deviation extracted (figure 7). Because the mold is likely tilted slightly from normal in the SEM image, either due to tilt of the sample itself or of the electron beam, the fit may be to an ellipse instead of a circle to remove the tilt-related distortion.

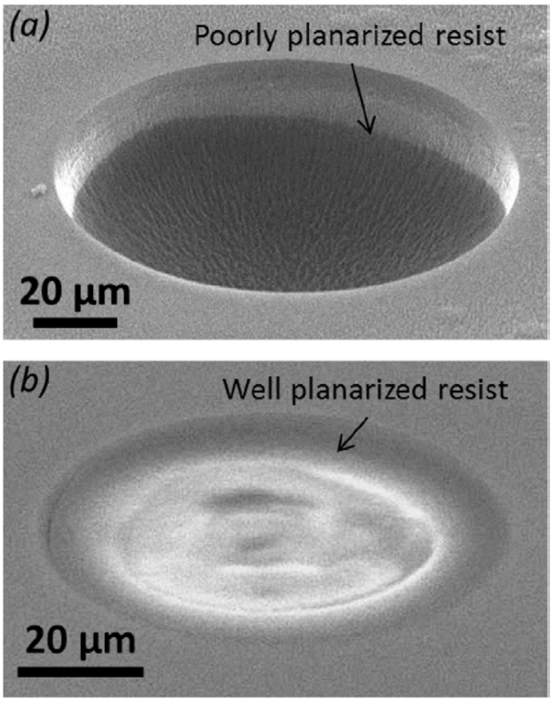

Figure 8. (*a*) An example of a single coat of resist etched with an O_2 plasma at 1 Torr, displaying hardened resist residue and a poorly planarized mold. (*b*) An example of three coats of resist, each etched with an O_2 plasma at 10 Torr, leaving behind no residue and a well-planarized mold.

An example of both circular and elliptical fits for a given mold can be seen in figure 7(*b*). The elliptical fit (red line) provides a lower limit to the radial error of 0.13 μm, while the circular fit (black line) provides an upper limit of 0.28 μm. Thus, given a radius of 57.4 μm, the radius is uniform to within 0.22–0.49%, indicating a highly symmetric mold. Additionally, the elliptical fit reveals the threefold symmetry associated with the Si (1 1 1) crystal planes [8], indicating that the HNA etch still has some slight crystal orientation dependence and could be optimized further.

3.2. ALD shell definition

After mold fabrication, the next task is to deposit and pattern the ALD Al_2O_3, as shown in figures 5(*c*) and (*d*). The Al_2O_3 is deposited at 130 °C using trimethylaluminum and water as precursors, in a procedure described elsewhere [20]. To pattern the ALD film, a thick photoresist is spun on the wafers and etched back in an O_2 plasma until the molds are planarized. The Al_2O_3 is then etched from the substrate while the molds are protected by the resist. After the Al_2O_3 etch, the resist is removed to leave unsuspended ALD shells.

The resist must be well-planarized to prevent exposing any part of the Al_2O_3 shell to the Al_2O_3 etch. The type of resist, as well as its spin speed conditions, heavily influences the quality of planarization. The best planarization was provided by 3–5 repetitions of the spin and etch-back process, using AZ-9260 resist nominally spun at a thickness of ~10 μm. Fewer coatings of a thicker resist resulted in problems with resist bubbling, while more coatings of a thinner resist caused extensive cracking due to the repeated thermal cycling. Larger molds also experience more problems with resist bubbling, limiting the current maximum mold radius to 50–60 μm. Larger shells will require either a further-optimized planarization process or an alternate etch technique (such as chemical mechanical polishing).

The resist etch-back conditions also play a large role in the quality of the planarization. When etching the photoresist with an O_2 plasma at pressures ranging from 10 mTorr to 1 Torr, the photoresist does not etch uniformly or cleanly, resulting in hardened resist debris and an uneven thickness, as seen in figure 8(*a*). By switching to a barrel asher operating at 10 Torr and an elevated temperature (up to 200 °C), no residue remained and the height of the resist stayed constant, as in figure 8(*b*). With the molds properly protected, the uncovered ALD material is etched using a buffered HF solution.

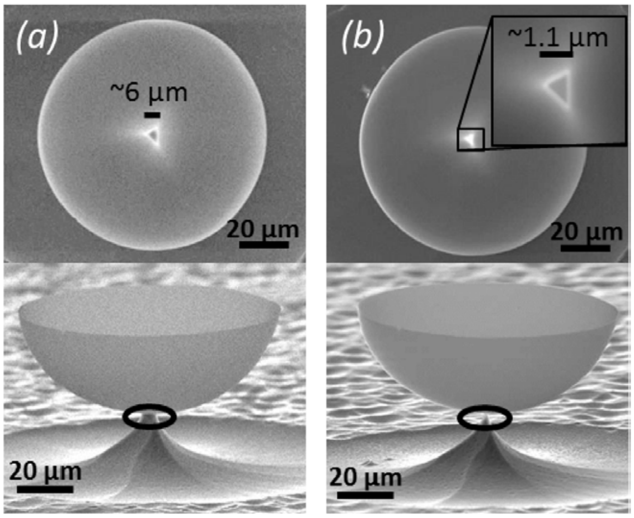

Figure 9. SEM micrographs showing sequential narrowing of a shell's anchor from a radius of 3 μm (*a*) to 0.6 μm (*b*) after additional Si etching.

3.3. Shell release

The final step of the wineglass fabrication is to release the shell from the surrounding substrate, defining the wineglass anchor. The anchor radius r_a largely determines Q_{anch} and, if too large, can limit Q to ~100. Fortunately, this fabrication scheme provides accurate control over r_a.

The anchor control is provided by a timed Si etch, using an SF_6 inductively coupled plasma (ICP) with the platen power set to 0 W to reduce physical ablation of the Al_2O_3. Initially, the Si etch is timed for an approximate target anchor radius. Because the Al_2O_3 is transparent, imaging the shells from overhead with an optical microscope clearly reveals the width of the anchor under the shell. If the anchor is not yet to the desired size, the wafer can be re-etched with shorter and shorter time intervals. Using this technique, anchors with radii between 0.5 and 1 μm can consistently be fabricated, as seen in figure 9. The anchors exhibit triangular or hexagonal

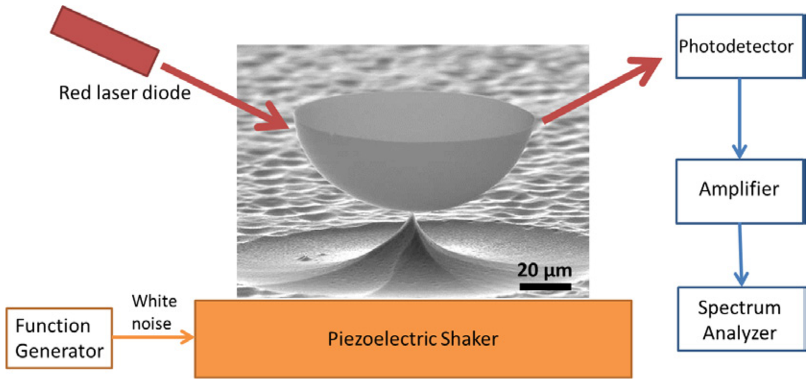

Figure 10. Schematic of the optical resonance measurement technique, as described in the text.

cross-sections indicative of the Si (1 1 1) crystal planes, due to the crystal-orientation-dependent SF_6 etch.

4. Measurement

After the shells were fabricated, their resonance characteristics were measured via an optical reflection technique. A schematic of the measurement setup is provided in figure 10. Briefly, the shells are driven into resonance by mechanical coupling to a lead–zirconate–titanate (PZT) piezoelectric shaker driven by broadband white noise. A laser diode (670 nm) reflects off of the shell at grazing incidence (~80° from normal) and is measured by a photodetector. The resulting signal is amplified and processed with a Fourier transform by a spectrum analyzer. All data is taken under vacuum at 10^{-5} Torr and at room temperature.

Figure 11 shows two example measurements from the same shell, before and after its anchor is thinned from r_a = 7 to 3 μm. The Lorentzian fit to the thick-anchor data reveals f_0 = 68.71 kHz and Q = 230, while the thin-anchor data shows f_0 = 58.54 kHz and Q = 1270. The improvement in Q implies that as the anchor is thinned, the impact of anchor loss is reduced, in agreement with the trend from the FEM model in figure 4. Subsequently, r_a was thinned again, from 3 to 0.6 μm, with no corresponding improvement in Q. The lack of improvement implies that anchor loss is no longer the dominant contributing factor to Q. Some possible alternate dissipation mechanisms are proposed in section 5, below.

Resonance frequency is also a function of anchor width, and there is a discrepancy in the modeled versus measured f_0. For r_a = 7 μm, the FEM model predicts f_0 = 62 kHz, 10% lower than the measured 68.71 kHz, while for r_a = 3 μm, the error increases to 25% (44 versus 58.54 kHz). The most likely explanation for this discrepancy is residual stress: ALD Al_2O_3 is known to have a relatively high residual stress, around 400 MPa when grown at 130 °C [24], which can shift f_0 substantially from the unstressed case. For the case of the shell in figure 11, the closest match to the resonances of both anchor widths was provided by including 120 MPa residual stress in the FEM model, for which the predicted frequencies are 73 kHz and 55 kHz for r_a = 7 μm and 3 μm, respectively, improving the error to 6% in both cases (down from 10 and

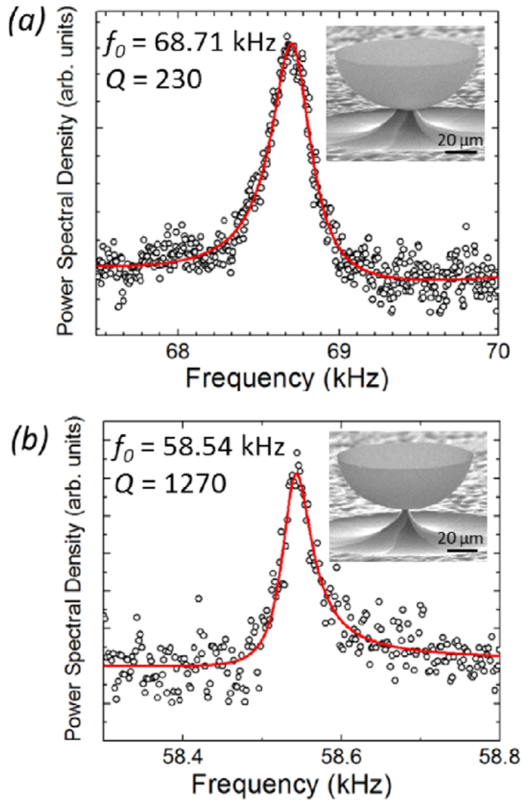

Figure 11. Example resonance peak, taken at 10^{-5} Torr and room temperature, from a 52 nm thick, 48 μm radius Al_2O_3 shell from before (*a*) and after (*b*) its anchor is thinned from a radius of 7–3 μm. The thinner anchor increases Q by 5.5 × , from 230 to 1270, and decreases f_0 from 68.71 to 58.54 kHz. Insets: SEM micrographs of the measured shell.

25%). The 120 MPa stress is lower than the expected 400 MPa, and may be an indication of stress relaxation in the suspended shell.

The preceding FEM analysis assumes the measured mode is the n = 2 wineglass mode. To verify whether the measured resonance modes are the expected lowest-order wineglass modes (and not, for example, the n = 3 mode or the n = 1 rocking mode), the resonance mode shapes were imaged inside an SEM. For this measurement, the shells are again driven with a PZT shaker, as in the optical technique, but instead of driving

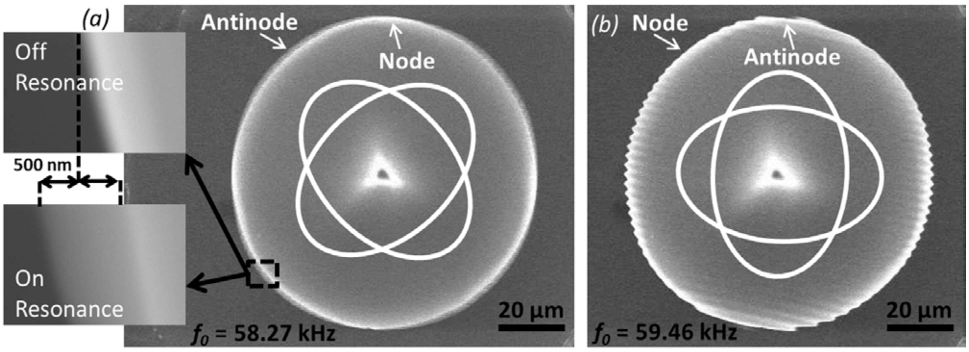

Figure 12. (*a*) Mode shape as seen in an SEM of the resonance measured in figure 11. Blurred regions indicate high amplitude antinodes, while stationary regions indicate nodes of the lowest order wineglass resonance (white lines). Inset: closeup of the stationary rim when off resonance and the blurred rim when on resonance, displaying an amplitude of vibration of ±500 nm. (*b*) The degenerate wineglass mode, where nodes and antinodes are rotated 45° from (*a*).

with white noise, the PZT is driven at a coherent frequency. This frequency is scanned through f_0; upon resonance, the shell's rim blurs and reveals the corresponding mode shape. Figure 12 shows an example of the visible mode shape of the same shell as seen in figure 11(*b*). The first mode occurs at 58.3 kHz, very near the 58.5 kHz measured optically, and the $n = 2$ mode shape (figure 2) is plainly visible, with nodes and antinodes evenly spaced every 45°. Further, the second (nominally degenerate) mode appears at 59.5 kHz—a mode not seen in the optical data, likely obscured by noise—with its standing wave rotated 45° compared to the first mode. The periodic distortion is likely due to aliasing between the shell's vibration and the scan rate of the SEM. This SEM technique confirms that the measured resonances are the two $n = 2$ wineglass modes.

It is worth noting that while the 1.2 kHz split between the two degenerate modes is relatively large, it is not necessarily accurate. As a consequence of measuring inside an SEM, the shell is undergoing competing effects of mass-loading-induced softening (from electron beam induced deposition [32]) and electrostatic stiffening, and as such, its resonance frequencies are asymmetrically drifting. Thus, the optical technique is required to measure accurate Δf values. Figure 13 shows an example of the mode splitting of a different device measured optically, showing Δf = 100 Hz, corresponding to a relative split of 0.3%. This split is likely due to a combination of the measured asymmetry in the mold geometry, fabrication-induced defects in the Al_2O_3 (causing, for example, local variations in Young's modulus), and surface contamination (causing local variations in density).

This SEM technique reveals that the Al_2O_3 shells are robust enough that they may be driven to an amplitude of >500 nm, or more than 10 × the thickness of the device itself, without tearing or dislodging from their anchors. An approximate Q can be extracted from the frequencies at which the amplitude reaches half its maximum. This shell displayed an approximate full width at half maximum of ~50 Hz, corresponding to a Q of ~1200, which is in good agreement with the 1270 measured optically in figure 11(*b*).

This agreement in Q implies that, even with such a large displacement amplitude, the resonator is not being over-driven

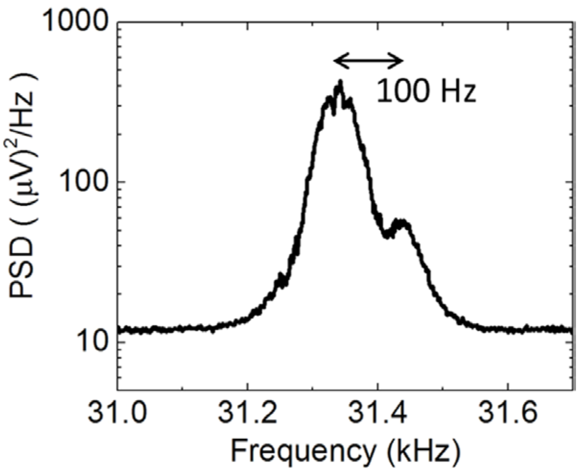

Figure 13. Example of the mode splitting between the lowest-order degenerate wineglass modes, with Δf = 100 Hz, or 0.3%.

to the point of causing nonlinear broadening. To ensure the optical measurement is also not broadened nonlinearly, Q was measured at different drive voltages and was consistent. Furthermore, the drive for the optical measurement is two to three orders of magnitude lower than the drive in the SEM. This lower drive implies that the displacement amplitudes for the optical data should be between 0.5 and 5 nm, presumably well within the linear regime for a 50 nm thick device. In total, five different shells were measured optically, each with Q values between 1000 and 2000.

5. Discussion

The measured Qs of 1000–2000 are well below the modeled Q_{anch} and Q_{TED} predictions of 10^6. This discrepancy implies that anchor loss and TED are not the principal energy dissipation mechanisms in these shells, although further refinement of the FEM accuracy is needed to more definitively discount these loss mechanisms. The next most likely sources of energy dissipation are from defects and surface effects.

Defects cause loss either through defect motion [33] or acoustic scattering [34]. The fabrication process might be inducing defects in the shells that reduce Q, an effect that has previously been seen on torsional silicon micro-resonators [35]. The damage could occur either during the Al_2O_3 buffered HF etch or the Si SF_6 release etch. For example, HF is known to diffuse through photoresist and so might attack the masked shell, particularly through cracks in the resist, while the Si SF_6 release etch might cause some amount of physical ablation despite the absence of platen power. These defects could potentially be reduced or eliminated by modifying the fabrication process, for example, by changing the Al_2O_3 etch from buffered HF to ion milling or chemical mechanical polishing, and changing the Si release etch from an SF_6 plasma to a XeF_2 gas.

The other likely source of energy dissipation is from surface effects. As the thickness of a resonator decreases, its surface-to-volume ratio increases, increasing the contribution of surface effects on total energy loss relative to volume effects. For example, surfaces contribute additional phonon scattering mechanisms, resulting in a decrease in Q [29]. This effect could be investigated by fabricating shells of different thicknesses: as thickness increases surface effects become less important, meaning Q should increase if the surface is dominating energy loss.

6. Conclusions

ALD wineglass micro-resonators were successfully fabricated by first etching hemispherical molds in Si (1 1 1) with HNA, then conformally coating and patterning the molds with ALD Al_2O_3, and finally releasing the Al_2O_3 shells from the surrounding substrate. Radii typically were ~50 μm with thicknesses of ~50 nm. The shells are supported by Si stems that were consistently fabricated with radii around 0.5 μm. Because of the high conformality of ALD, this fabrication process is extendable to applications with arbitrarily shaped 3D molds.

The shells' resonance properties were measured through an optical reflection technique, revealing typical resonance frequencies around 60 kHz, with quality factors between 1000 and 2000. An SEM imaging technique revealed the shells' resonance mode shapes by driving the resonances at an amplitude 10 times their thickness, without causing any structural damage. Finite element modeling predicted that anchor loss and thermoelastic dissipation would lead to quality factors over 10^6. The measured Q of only 10^3 suggests that alternative energy dissipation mechanisms are dominating. The most likely sources of dissipation are from defects and surface effects, which could be investigated further by modifying the fabrication process to reduce defects and increasing ALD thickness to reduce surface effects. Such studies will be important to achieve the high Q (10^6–10^7) necessary for utilizing hemispherical micro-resonators as high-precision gyroscopes.

Acknowledgments

This material is based upon work supported by the DARPA Microscale Rate Integrating Gyroscope (MRIG) program under grant N66001-13-1-4028. Microfabrication and SEM imaging were performed at the Colorado Nanofabrication Laboratory (CNL) and the Nanomaterials Characterization Facility (NCF) of the University of Colorado, Boulder.

References

[1] Rozelle D M 2009 The hemispherical resonator gyro: from wineglass to the planets *Proc. 19th AAS/AIAA Space Flight Mechanics Meeting* (*Savannah, GA,* 8–12 February 2009) pp 1157–78

[2] Shkel A M 2006 Type I and type II micromachined vibratory gyroscopes *Proc. IEEE/ION Position, Location, and Navigation Symp*. (*San Diego, CA,* 25–27 April 2006) pp 586–93

[3] Gallacher B J 2012 Principles of a micro-rate integrating ring gyroscope *IEEE Trans. Aerosp. Electron. Syst*. **48** 658–72

[4] Matthews A D and Bauer D A 1995 Hemispherical resonator gyro for precision pointing applications *Proc. SPIE* **2466** 128–41

[5] Meyer A D and Rozelle D M 2012 Milli-HRG inertial navigation system *Gyrosc. Navigation* **3** 227–34

[6] Matthews A and Rybak F J 1992 Comparison of hemispherical resonator gyro and optical gyros *IEEE Aerosp. Electron. Syst. Mag.* **7** 40–6

[7] Izmailov E A, Kolesnik M M, Osipov A M and Akimov A V 1999 Hemispherical resonator gyro technology. Problems and possible ways of their solutions *Proc. RTO SCI International Conf. on Integrated Navigation Systems* (*St. Petersburg, Russia*, 24–26 May 1999) p 6.1–6.9

[8] Bernstein J J, Bancu M G, Cook E H, Chaparala M V, Teynor W A and Weinberg M S 2013 A MEMS diamond hemispherical resonator *J. Micromech. Microeng.* **23** 125007

[9] Woo J, Cho J Y, Boyd C and Najafi K 2014 Whole-angle-mode micromachined fused-silica birdbath resonator gyroscope *Proc. IEEE 27th Int. Conf. on Micro Electro Mechanical Systems* (*San Francisco, CA*, 26–30 January 2014) pp 20–3

[10] Senkal D, Ahamed M J, Trusov A A and Shkel A M 2013 High temperature micro-glassblowing process demonstrated on fused quartz and ULE TSG *Sensors Actuators* A **201** 525–31

[11] Shao P, Tavassoli V, Liu C, Sorenson L and Ayazi F 2014 Electrical characterization of ALD-coated silicon dioxide micro-hemispherical shell resonators *Proc. IEEE 27th Int. Conf. on Micro Electro Mechanical Systems* (*San Francisco, CA*, 26–30 January 2014) pp 612–5

[12] Heidari A, Chan M, Yang H, Jaramillo G, Taheri-Tehrani P, Fonda P, Najar H, Yamazaki K, Lin L and Horsley D A 2013 Hemispherical wineglass resonators fabricated from the microcrystalline diamond *J. Micromech. Microeng.* **23** 125016

[13] Rahman M M, Xie Y, Mastrangelo C and Kim H 2014 3-d hemispherical micro glass-shell resonator with integrated electrostatic excitation and capacitive detection transducers *Proc. IEEE 27th Int. Conf. on Micro Electro Mechanical Systems* (*San Francisco, CA*, 26–30 January 2014) pp 672–5

[14] George S M 2010 Atomic layer deposition: an overview *Chem. Rev.* **110** 111–31

[15] Ritala M, Leskela M, Dekker J P, Mutsaers C, Soininen P J and Skarp J 1999 Perfectly conformal TiN and Al_2O_3 films deposited by atomic layer deposition *Chem. Vapor Depos.* **5** 7–9

[16] Carcia P F, Mclean R S, Reilly M H, Groner M D and George S M 2006 Ca test of Al_2O_3 gas diffusion barriers

grown by atomic layer deposition on polymers *Appl. Phys. Lett*. **89** 031915
[17] Fabreguette F H, Sechrist Z A, Elam J W and George S M 2005 Quartz crystal microbalance study of tungsten atomic layer deposition using WF_6 and Si_2H_6 *Thin Solid Films* **488** 103–10
[18] Hoivik N D, Elam J W, Linderman R J, Bright V M, George S M and Lee Y C 2003 Atomic layer deposited protective coatings for micro-electromechanical systems *Sensors Actuators* A **103** 100–8
[19] Wilson C A, Grubbs R K and George S M 2005 Nucleation and growth during Al_2O_3 atomic layer deposition on polymers *Chem. Mater.* **17** 5625–34
[20] Groner M D, Fabreguette F H, Elam J W and George S M 2004 Low-temperature Al_2O_3 atomic layer deposition *Chem. Mater.* **16** 639–45
[21] Wind R W, Fabreguette F H, Sechrist Z A and George S M 2009 Nucleation period, surface roughness, and oscillations in mass gain per cycle during W atomic layer deposition on Al_2O_3 *J. Appl. Phys.* **105** 074309
[22] Yasumura K Y, Stowe D, Chow E M, Pfafman T, Kenny T W, Stipe B C and Rugar D 2000 Quality factors in micron- and submicron-thick cantilevers *J. Microelectromech. Syst.* **9** 117–25
[23] Senkal D, Raum C R, Trusov A A and Shkel A M 2012 Titania silicate/fused quartz glassblowing for 3-d fabrication of low internal loss wineglass micro-structures *Proc. Solid-State Sensors, Actuators, and Microsystems Workshop Digest* (*Transducers Research Foundation, Hilton Head Island, SC,* 3–7 June 2012) pp 267–70
[24] Ylivaara O M E *et al* 2014 Aluminum oxide from trimethylaluminum and water by atomic layer deposition: the temperature dependence of residual stress, elastic modulus, hardness and adhesion *Thin Solid Films* **552** 124–35
[25] Miller D C, Foster R R, Jen S, Bertrand J A, Cunningham S J, Morris A S, Lee Y, George S M and Dunn M L 2010 Thermo-mechanical properties of alumina films created using the atomic layer deposition technique *Sensors Actuators* A **164** 58–67
[26] Gorham C S, Gaskins J T, Parsons G N, Losego M D and Hopkins P E 2014 Density dependence of the room temperature thermal conductivity of atomic layer deposition-grown amorphous alumina (Al_2O_3) *Appl. Phys. Lett.* **104** 253107
[27] Srikar V T and Senturia S D 2002 Thermoelastic damping in fine-grained polysilicon flexural beam resonators *J. Microelectromech. Syst.* **11** 499–504
[28] Bindel D S and Govindjee S 2005 Elastic PMLs for resonator anchor loss simulation *Int. J. Numer. Methods Eng.* **64** 789–818
[29] Kunal K and Aluru N R 2011 Akhiezer damping in nanostructures *Phys. Rev.* B **84** 245450
[30] Schwartz B and Robbins H 1976 Chemical etching of silicon IV. Etching technology *J. Electrochem. Soc.* **123** 1903–9
[31] Hamzah A A, Aziz N A, Majilis B Y, Yunas J, Dee C F and Bais B 2012 Optimization of HNA etching parameters to produce high aspect ratio solid silicon microneedles *J. Micromech. Microeng.* **22** 095017
[32] van Dorp W F and Hagen C W 2008 A critical literature review of focused electron beam induced deposition *J. Appl. Phys.* **104** 081301
[33] Mohanty P, Harrington D A, Ekinci K L, Yang Y T, Murphy M J and Roukes M L 2002 Intrinsic dissipation in high-frequency micromechanical resonators *Phys. Rev.* B **66** 085416
[34] Lee S, Yoon K H and Lee J 2002 Influence of electrode configurations on the quality factor and piezoelectric coupling constant of solidly mounted bulk acoustic wave resonators *J. Appl. Phys.* **92** 4062
[35] Mihailovich R E and MacDonald N C 1995 Dissipation measurements of vacuum-operated single-crystal silicon microresonators *Sensors Actuators* A **50** 199–207